Table IV

atom	orbital	H_{ii}, eV	ζ
In	5s	-12.60	1.903
	5p	-6.19	1.677
Ga	4s	-14.58	1.77
	4p	-6.75	1.55

participate in the skeletal bonding. The appropriate electron count (eight pairs) can only be obtained if one of the carbons in the ring is substituted by one boron. So, 14 is a likely candidate. One of the metal atoms in 14 could

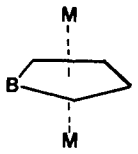

14

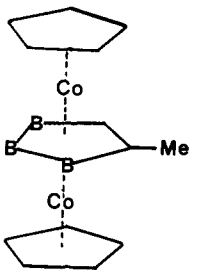

15

be substituted by an Sn-R group without changing the electron count. With use of the isolobal analogy, one of the metals can be substituted by a group like FeCp and the bonding characteristics are not altered, or conversely we could use a CoCp group and substitute another carbon atom by a boron in the central cyclopentadienyl. Substitution of the remaining M by another CoCp and replacing another carbon by a boron, without altering the number of skeletal electrons, give us the well-known $Co_2Cp_2(3\text{-}CH_3\text{-}2,3\text{-}C_2B_3H_4)$ (**15**). These inverse sandwich structures are then the inorganic equivalent of the triple-decker compounds. A rich chemistry of indium and thallium is probably still uncovered.

Acknowledgment. We are grateful to Dr. J. C. Barthelat for providing a copy of the PSHONDO program. We are grateful to Professor J. K. Burdett for helpful discussions. E.C. thanks the Department of Chemistry of the University of Michigan for their hospitality. O.E. acknowledges the donors of the Petroleum Research Fund, administered by the American Chemical Society, for support of this research.

Appendix

The exponents and parameters for In and Ga were taken from Clementi and Roetti[41] and Hinze and Jaffe,[42] respectively. The modified Wolfsberg-Helmholtz formula was used.[43] The parameters for *B* and *C* were the standard ones.[44] Distances C-C = 1.42 Å and C-H = 1.08 Å were used for cyclopentadienyl. The experimental Cp-In distances were used for monomeric (2.32 Å) and polymeric (3.19 Å) CpIn. Experimental structural data[40] were used for $1\text{-}CH_3GaC_2B_4H_6$ (Table IV).

Registry No. 1, 34822-89-4; CpTl, 34822-90-7; $CpSn^+$, 77220-40-7.

(41) Clementi, E.; Roetti, C. *At. Data Nucl. Data Tables* **1974**, *14*, 177.
(42) Hinze, J.; Jaffe, H. H. *J. Phys. Chem.* **1963**, *67*, 1501.
(43) Ammeter, J. H.; Bürgi, H.-B.; Thibeault, J.; Hoffmann, R. *J. Am. Chem. Soc.* **1978**, *100*, 3686.
(44) Hoffmann, R. *J. Chem. Phys.* **1963**, *39*, 1397.

The Unusual Bonding Capabilities of a Tetrametal Butterfly Cluster Fragment: Electronic Structures of $HFe_4(CO)_{12}CH$ and $HFe_4(CO)_{13}^-$

Thomas P. Fehlner and Catherine E. Housecroft*

Department of Chemistry, University of Notre Dame, Notre Dame, Indiana 46556

Received October 18, 1983

Different coordination geometries of the CH^- and CO^{2-} ligands on the tetrairon butterfly cluster $HFe_4(CO)_{12}^+$ are explored by using the Fenske-Hall quantum chemical technique. The known preference for η^2 rather than η^1 ligand binding is examined for both. It is demonstrated that the complexes $HFe_4(CO)_{12}CH$ and $HFe_4(CO)_{13}^-$ are aptly described as having a primary triiron-CH or triiron-CO core, thereby supporting a simple geometrical analysis of their structures. Possible mechanisms for the weakening of the ligand C-H and C-O bonds in these complexes in going from η^1 to η^2 geometries are presented and compared. The results suggest that the versatile nature of the metal butterfly causes the CO^{2-} ligand to be increasingly activated on tilting primarily by loss of charge from a CO π-binding orbital, whereas the CH^- ligand is activated both by charge loss from filled CH σ-bonding orbitals and by charge transfer into a CH σ-antibonding orbital. The major contributory factor to this mechanistic difference is the lack of dinuclear π orbitals on CH. Finally, the difference between the η^2 and η^1 geometries for CH^- are subtle ones whereas those for CO^{2-} are more obvious.

The class of compound in which a main-group "ligand" bridges the wingtips of a homonuclear tetrametal butterfly cluster fragment is becoming increasingly exemplified.[1-7] Clusters of the type $HFe_4(CO)_{12}X$ can be formulated in terms of the metal fragment $HFe_4(CO)_{12}^+$ and, for example,

(1) (a) Tachikawa, M.; Muetterties, E. L. *J. Am. Chem. Soc.* **1980**, *102*, 4541. (b) Beno, M. A.; Williams, J. M.; Tachikawa, M.; Muetterties, E. L. *Ibid.* **1980**, *102*, 4542; **1981**, *103*, 1485.
(2) Whitmire, K. H.; Shriver, D. F. *J. Am. Chem. Soc.* **1981**, *103*, 6754. Holt, E. M.; Whitmire, K. H.; Shriver, D. F. *J. Organomet. Chem.* **1981**, *213*, 125.
(3) Bradley, J. S.; Ansell, G. B.; Hill, E. W. *J. Am. Chem. Soc.* **1979**, *101*, 7418. Bradley, J. S.; Ansell, G. B.; Leonwicz, M. E.; Hill, E. W. *Ibid.* **1981**, *103*, 4968.
(4) Fjare, D. E.; Gladfelter, W. L. *Inorg. Chem.* **1981**, *20*, 3532.
(5) Manssero, M.; Sansoni, M.; Longoni, G. *J. Chem. Soc., Chem. Commun.* **1976**, *919*.
(6) Fehlner, T. P.; Housecroft, C. E.; Scheidt, W. R.; Wong, K. S. *Organometallics* **1983**, *2*, 825.

0276-7333/84/2303-0764$01.50/0

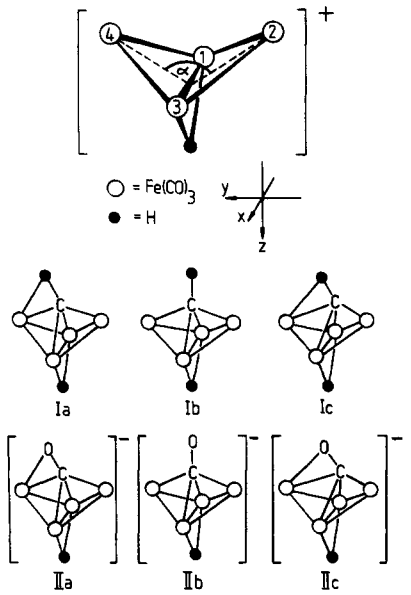

Figure 1. Structure of the $HFe_4(CO)_{12}^+$ fragment in complexes of type $HFe_4(CO)_{12}X$, showing Fe atom numbering, internal dihedral angle α, and axis system. For X = CH^- (I) and CO^{2-} (II), structures a and b have C equidistant between the wing tip Fe atoms; structure c has C slipped off the C_2 axis of the metal butterfly as found experimentally.

the ligand CH^- or CO^{2-} (Figure 1). One great interest in such clusters is their relationship to metal surface bound main-group fragments. The skeletal butterfly geometry of the metal unit in $HFe_4(CO)_{12}^+$ as derived from $HFe_4(CO)_{12}CH$ (I) or $HFe_4(CO)_{13}^-$ (II) approximates that of a "step" surface M_4 site developed at the intersection of two 111 faces in a close packed array of metal atoms. The internal dihedral angle (α in Figure 1) is 111° in I, 117° in II, and 109° in the bulk metal. Although other sites are available on a metal surface, the stepped sites appear to possess enhanced reactivity.[8] Still, experimental and theoretical studies of the mode of attachment of the CH unit to a metal 111 surface have been inconclusive in determining whether the C–H bond vector coincides or not with the 3-fold axis of a triangular M_3 adsorption site.[9] Vector/axis coincidence would lead to an M_3CH core akin to that characterized crystallographically in a number of clusters.[10] Tilting the CH vector with respect to the C_3 axis prepares the H atom of the CH for interaction with a surface metal atom, a mechanism that is assumed to initiate C–H bond activation and ultimate scission.[11-13] The beauty of the four-atom butterfly site is that it encompasses both a triangular metal unit in one of the butterfly wings and an adjacent metal atom positioned for a secondary M–H–C interaction (Figure 2). I (Figure 1) illustrates this mode of ligand attachment and exhibits a long (1.19 Å) C–H bond.[1] Thus, I has been suggested as a model of a CH fragment with the CH bond weakened (activated) by interaction with surface metal atoms.[13] Other examples of compounds with C–H–M bonds have been reviewed.[14]

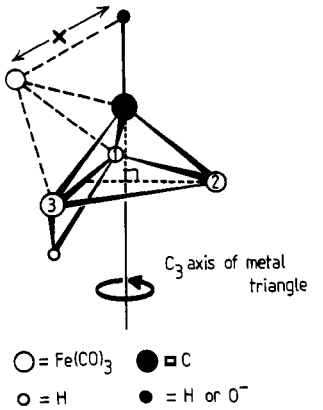

Figure 2. Generation of Ia and IIa by the facial capping of $HFe_3(CO)_9X^-$ (X = CH^- or CO^{2-}) by $Fe(CO)_3^{2+}$.

Chart I

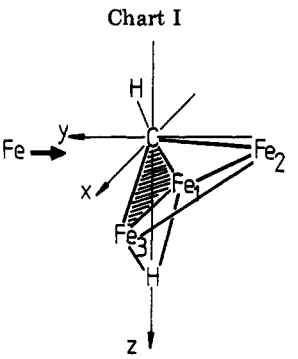

The Fischer–Tropsch reaction has been and is the subject of numerous research studies,[15,16] and the cluster analogy has been applied here as well. For example, the proton-induced reduction of CO to CH_4[17] has been demonstrated starting with $Fe_4(CO)_{13}^{2-}$, which on initial protonation gives $HFe_4(CO)_{13}^-$ (II). II, like I, has a ligand (this time CO) asymmetrically bridging the wing tips of a tetrairon butterfly fragment (Figure 1).[5] Coordination of CO to a metal in general weakens the CO bond by back-donation of charge from filled metal to empty CO π^* orbitals. It is also established that the C–O bond of a μ_3-carbonyl is longer and weaker than that of a μ_2-carbonyl but that in II is even longer (1.26 Å).[5] Thus, further protonation leads to C–O bond cleavage and subsequent formation of CH_4.[17] Intermediate in this reaction sequence is the metal carbide $HFe_4(CO)_{12}C^-$ which protonates easily to yield I. Recent work shows that the reactivity of metal carbide centers can be correlated with their degree of exposure.[3a,18-21] The carbide in the Fe_4C environment is more reactive than that in the Fe_6C and Fe_5C structures. Thus, the tetrametal butterfly site has sufficient metal atoms to facilitate main-group-fragment activation but not too many to inhibit approach of a reacting partner.

Using I and II as model compounds, we have investigated the bonding capabilities of the tetrairon butterfly in the form of the cluster fragment $HFe_4(CO)_{12}^+$ and have

(7) Carty, A. J.; MacLaughlin, S. A.; Van Wagner, J.; Taylor, N. *Organometallics* **1982**, *1*, 1013.
(8) Anderson, A. B.; Hoffmann, R. *J. Chem. Phys.* **1974**, *61*, 4545.
(9) DeKock, R. L.; Fehlner, T. P. *Surf. Sci.* **1982**, *119*, 391 and references therein.
(10) See for example: Raithby, P. R. In "Transition Metal Clusters"; Johnson, B. F. G., Ed.; Wiley: New York, 1980; p 5.
(11) Deeming, A. J. In "Transition Metal Clusters"; Johnson, B. F. G., Ed.; Wiley: New York, 1980; p 391.
(12) Muetterties, E. L. *Chem. Rev.* **1983**, *83*, 283.
(13) Gavin, R. M.; Ruett, J.; Muetterties, E. L. *Proc. Natl. Acad. Sci. U.S.A.* **1981**, *78*, 3981.
(14) Brookhart, M.; Green, M. L. H. *J. Organomet. Chem.* **1983**, *250*, 395 and references therein.
(15) Ugo, R.; Psaro, R. *J. Mol. Catal.* **1983**, *20*, 53.
(16) Shriver, D. F. *Chem. Br.* **1983**, *19*, 484.
(17) Drezdzon, M. A.; Whitmire, K. H.; Bhattacharyya, A. A.; Hsu, W.-L.; Nagel, C. C.; Shore, S. G.; Shriver, D. F. *J. Am. Chem. Soc.* **1982**, *104*, 5630.
(18) Tachikawa, M.; Muetterties, E. L. *Prog. Inorg. Chem.* **1981**, *28*, 203.
(19) Muetterties, E. L.; Stein, J. *Chem. Rev.* **1979**, *79*, 479.
(20) Kolis, J. W.; Basolo, F.; Shriver, D. F. *J. Am. Chem. Soc.* **1982**, *104*, 5626.
(21) Sosinsky, B. A.; Norem, N.; Shelly, J. *Inorg. Chem.* **1982**, *21*, 348.

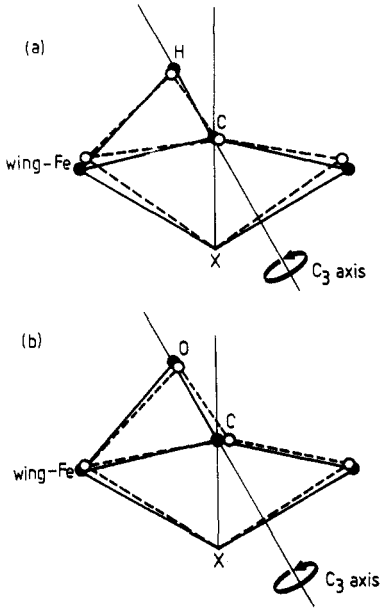

Figure 3. Cuts through (a) I and (b) II in the plane containing wing tip Fe and ligand atoms to compare the experimentally determined atomic positions with those calculated. Filled circles refer to calculated positions and open circles to experimental positions. The C_3 axis refers to the metal triangle as defined in Figure 2. Both cuts are drawn for Fe–C distances of 2.0 Å (see text).

explored the possible mechanisms of bond activation for different coordination geometries of the ligands CH^- and CO^{2-}. To this end we initially describe the structures of I and II in terms of a simple, geometrical model that emphasizes the metal butterfly as a source of a *trimetal* unit to which the ligand can bind strongly. Secondly, we use the Fenske–Hall[22] technique to probe metal-fragment–ligand bonding in terms of orbital energetics, orbital symmetries, Mulliken overlap populations, and Mulliken population changes. We have previously outlined the way in which CH^- and $HFe_4(CO)_{12}^+$ interact[23] but expand our arguments fully here.

Results and Discussion

I. Geometrical Analysis. $HFe_4(CO)_{12}CH$. The number of complexes containing an M_3CH core with the CH triply bridging three metal atoms that have been structurally characterized[10] suggest an energetic preference for the μ_3 orientation.[24,25] Formally, $HFe_4(CO)_{12}CH$ can be generated by capping one triangular face of the triiron–carbon tetrahedral core of an $HFe_3(CO)_9CH^{2-}$ residue (derived from $H_3Fe_3(CO)_9CR$) by an $Fe(CO)_3^{2+}$ fragment (Chart I). Using structural parameters from $H_3Fe_3(CO)_9CCH_3$[26a] (Fe–Fe = 2.62, Fe–C = 1.95 Å) and a C–H distance of 1.19 Å,[1] a model geometry for I was constructed (Figure 2). The calculated Fe(wing)–H distance (x in Figure 2) was 1.82 Å compared to 1.75 Å obtained experimentally.[1] Shortening the Fe–C bonds from 1.95 Å to 1.90 Å gives a calculated value of x = 1.68 Å. Figure 3a shows a cut through Ia in the plane containing the Fe(wing) and CH atoms. There is good agreement between the experimentally determined positions of these atoms and those calculated as detailed above. This model generates a tetrairon butterfly with a dihedral angle α of 116.8° (Fe–C = 1.95 Å) or 119.5° (Fe–C = 2.0 Å) vs. 111° in Ia.[1]

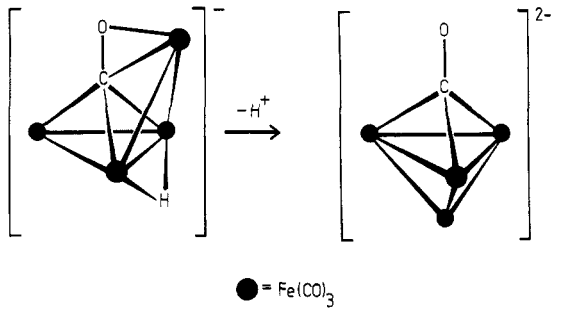

Figure 4. The structural change accompanying the deprotonation of $HFe_4(CO)_{13}^-$. The large filled circles represent $Fe(CO)_3$ units. Note that in $Fe_4(CO)_{13}^{2-}$ there are in fact three semibridging CO's.

$HFe_4(CO)_{12}CO^-$. When CO^- replaces CH in I, II results (Figure 1). This unique carbonyl is considered to be a four-electron donor to the cluster and asymmetrically bridges the tetrairon butterfly wing tips.[5] This mode of binding can be described qualitatively in terms of a carbonyl triply bridging one of the butterfly wings while π-binding to the fourth Fe atom.[5] The skeletal rearrangement that occurs when $HFe_4(CO)_{13}^-$ is deprotonated is illustrated in Figure 4, and it is noted that the unique CO retains its μ_3-bonding mode. II can be described as being derived from a $HFe_3(CO)_9(\mu_3\text{-}CO)^{3-}$ fragment which has the μ_3-CO lying along the C_3 axis of the triiron unit. Capping the Fe_1Fe_3C face of the tetrahedral triiron–carbon core (Figure 2) generates II in a geometry close to that found in practice (Figure 3b). Since the parent compound $H_3Fe_3(CO)_9(\mu_3\text{-}CO)^-$ has not been characterized, Fe–Fe and Fe–C distances of 2.62 and 1.95 Å were chosen to be consistent with $H_3Fe_3(CO)_9CCH_3$,[26a] and a C–O length of 1.26 Å[5] for the μ_3-CO was used. The imposed butterfly dihedral angle α of 116.8° compares favorably with an experimental value of 117° in II. The calculated wing tip Fe to oxygen distance of 1.84 Å is in quite good agreement with the experimental value of 2.00 Å.[5] If Fe–C = 2.0 Å, then calculated parameters are α = 119.5° and Fe–O = 1.97°. The most noticeable difference in the constructed and experimental geometries is the observed slippage (~0.19 Å) of the C atom toward one wing tip iron. This feature is less marked in the structure of I (~0.05 Å). With this exception, the correlation between constructed and real geometries for both I and II is quite striking.

In both I and II, the constructed geometry focuses exclusively on the binding of CH or CO^- perpendicularly to and lying along the C_3 axis of a triangular array of Fe atoms contained in one wing of the tetrametal butterfly, and the close agreement with the experimental geometries suggests that Ia and IIa retain a significant fraction of a triiron nonacarbonyl–methylidyne interaction.[26] Unless fortuitous, this begins to explain the geometrical preference of CH and CO^- with respect to the metal butterfly.

II. MO Fragment Analysis. Analyzing the modes of binding of two molecular fragments in a complex by examining the electronic properties of each fragment has become an informative way of understanding the fragment orbital interactions.[27,28] The Fenske–Hall technique[22] is

(22) Hall, M. B.; Fenske, R. F. *Inorg. Chem.* **1972**, *11*, 768. Hall, M. B. Ph.D. Thesis, University of Wisconsin, Madison, WI, 1971. Fenske, R. F. *Pure Appl. Chem.* **1971**, *27*, 61.
(23) Housecroft, C. E.; Fehlner, T. P. *Organometallics* **1983**, *2*, 690.
(24) Beurich, H.; Vahrenkamp, H. *Angew. Chem., Int. Ed. Engl.* **1981**, *93*, 128.
(25) Factors governing this preference can be outweighed as demonstrated in the structure of $HOs_3(CO)_{10}CH$: Shapley, J. R.; Cree-Uchiyama, M. E.; St. George, G. M.; Churchill, M. R., Bueno, C. *J. Am. Chem. Soc.* **1983**, *105*, 140.
(26) (a) Wong, K. S.; Haller, K. J.; Dutta, T. K.; Chipman, D. M.; Fehlner, T. P. *Inorg. Chem.* **1982**, *21*, 3197. (b) DeKock, R. L.; Wong, K. S.; Fehlner, T. P. *Ibid.* **1982**, *21*, 3203.
(27) Burdett, J. K. "Molecular Shapes. Theoretical Models of Inorganic Stereochemistry"; Wiley: New York, 1980.

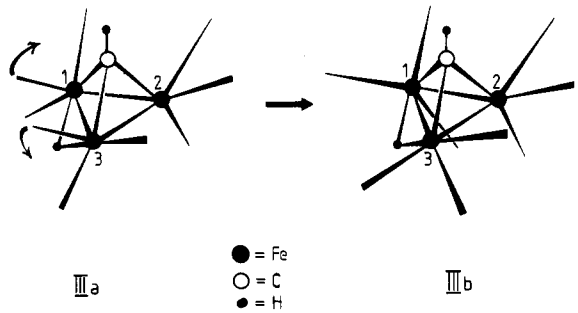

Figure 5. The structural change caused by iron tricarbonyl unit twisting that defines the transition from IIIa and IIIb. IIIa is $HFe_3(CO)_9CH^{2-}$ in a geometry taken directly from $H_3Fe_3(CO)_9CR$ and IIIb is the same trimetal fragment as it is incorporated into $HFe_4(CO)_{12}CH$. Note how the twisting action opens up the Fe_1Fe_3C face to attack.

particularly useful for relatively large metal-containing clusters since, after SCF covergence in the atomic basis set, the results can be transformed into a basis set of fragment molecular orbitals.[6,23,29] This simplifies the task of correlating individual fragment orbitals with those in the complex[30] and has the advantage of giving directly the fragment–fragment Mulliken overlap populations as well as a measure of the transfer of electronic charge from one fragment orbital to another. To support the simple geometrical model suggested above, Ia has been partitioned into the fragments $HFe_3(CO)_9CH^{2-}$ and $Fe(CO)_3^{2+}$. In addition, I and II are considered in terms of the interaction between $HFe_4(CO)_{12}^+$ and the ligand CH^-[23] or CO^{2-}. An alternative approach to the bonding in $HFe_4(CO)_{12}CH$ has been to consider the reactivity of the metal carbide $Fe_4(CO)_{12}C$ toward successive hydride addition, and Hoffmann et al. have rationalized the preference for Ia over other possible structures in terms of the nature of the HOMO's of the carbide fragment.[31] Throughout this work, fragment molecular orbitals will be referred to as "orbitals" to clearly distinguish them from those of the complex which will be termed "molecular orbitals" (MO's).

$HFe_3(CO)_9CH^{2-}$. In the geometrical analysis, the fragment $HFe_3(CO)_9CH^{2-}$ (III) was derived from $H_3Fe_3(CO)_9CCH_3$ which has three symmetrically positioned basal $Fe(CO)_3$ units, each with one CO pointing below the Fe_3 triangle and two CO's pointing above (structure IIIa in Figure 5). As far as accommodating the incoming $Fe(CO)_3^{2+}$ fragment, the carbonyl rearrangement illustrated in Figure 5 is necessary for steric reasons. The iron tricarbonyl units of atoms Fe_1 and Fe_3 in IIIa are twisted through 60° to generate IIIb, the $HFe_3(CO)_9CH^{2-}$ fragment in the geometry found in complex Ia. Orbital analyses of IIIa and IIIb indicate that the carbonyl twisting does more than simply make room for the $Fe(CO)_3^{2+}$ fragment. The filled orbitals of III (Figure 6) can be divided into a set of low-lying metal–carbonyl orbitals, a unique Fe–μ-H–Fe bridge bonding orbital (48),[32] six mainly metal containing orbitals (51–56) and triiron–alkylidyne cluster bonding orbitals (47,49,50,57–61) of which 61 is the HOMO. In Figure 6, the orbitals in IIIa are correlated with those in IIIb. Orbitals 47, 49, and 50 are the three orbitals mainly

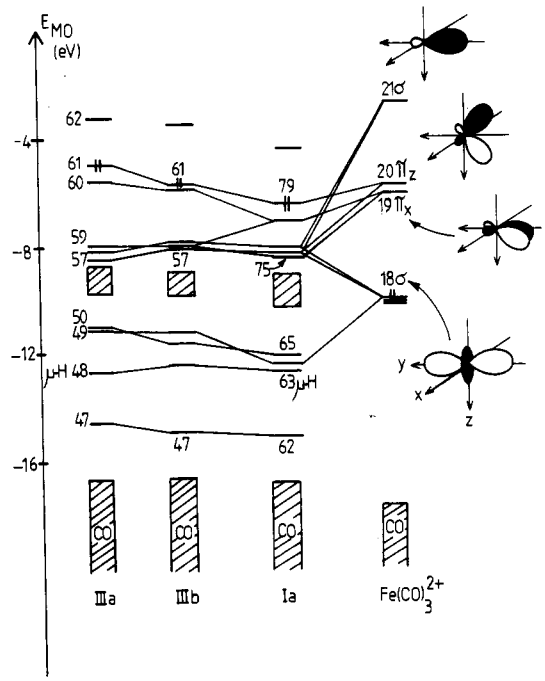

Figure 6. Fragment orbital correlation diagram for the formation of Ia from $HFe_3(CO)_9CH^{2-}$ and $Fe(CO)_3^{2+}$. The orbitals of the $HFe_3(CO)_9CH^{2-}$ fragment are correlated for the structural change IIIa to IIIb (Figure 5) that is required before the $HFe_3(CO)_9CH^{2-}/Fe(CO)_3^{2+}$ interaction can occur. The energy scale given is for the three right-hand columns;[30] the energies of the orbitals for IIIa are on the same scale as those of IIIb but arbitrarily positioned.

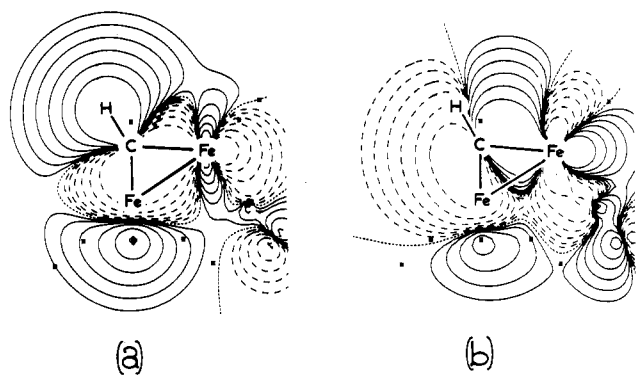

Figure 7. Amplitude contour plots for two of the principal triiron–alkylidyne bonding orbitals in $HFe_3(CO)_9CH^{2-}$: (a) orbital 47 and (b) orbital 50. Both are plotted in the *yz* plane containing Fe_2, C, and H atoms. The Fe_1 and Fe_3 atoms are out of plane but their midpoint is indicated on the plot; the vertical C–Fe line represents a cut through the Fe_1Fe_3C face. All other atoms either in or projected on to the specific plane are indicated by asterisks. Each diagram has six contours, each succeeding contour differing from the last by a factor of 2. The largest contour is 0.05 au^{-3}.

involved in binding the apical CH unit to the metal triangle[33] and are virtually unaffected in going from IIIa to IIIb; this justifies neglecting the carbonyl ligands in the geometrical argument which focused attention on the triiron–CH core. Figure 7 shows amplitude contour plots of orbitals 47 and 50. Changes in the characters of orbitals 57–59 and 61 in going from IIIa to IIIb are significant and are exemplified by the amplitude contour plots in Figure 8. Note that orbitals 61 (HOMO) and 59 of IIIb are beautifully set up for interactions with the $Fe(CO)_3^{2+}$ π_z and σ orbitals, respectively. In addition, comparison with

(28) Hoffmann, R. *Science (Washington DC)* **1981**, *211*, 995.
(29) Kostic, N. M.; Fenske, R. F. *Organometallics* **1982**, *1*, 974.
(30) The orbital energies of fragments are affected by the total fragment charge. A realistic comparison is made if the fragment orbital energies from the Fock matrix are used in conjunction with the eigenvalues for the complex itself as used here.[29]
(31) Hoffmann, R.; Wijeyesekera, S. D.; Wilker, C. N., personal communication.
(32) Mingos, D. M. P. *Pure Appl. Chem.* **1980**, *52*, 705.
(33) DeKock, R. L.; Wong, K. S.; Fehlner, T. P. *Inorg. Chem.* **1982**, *21*, 3203.

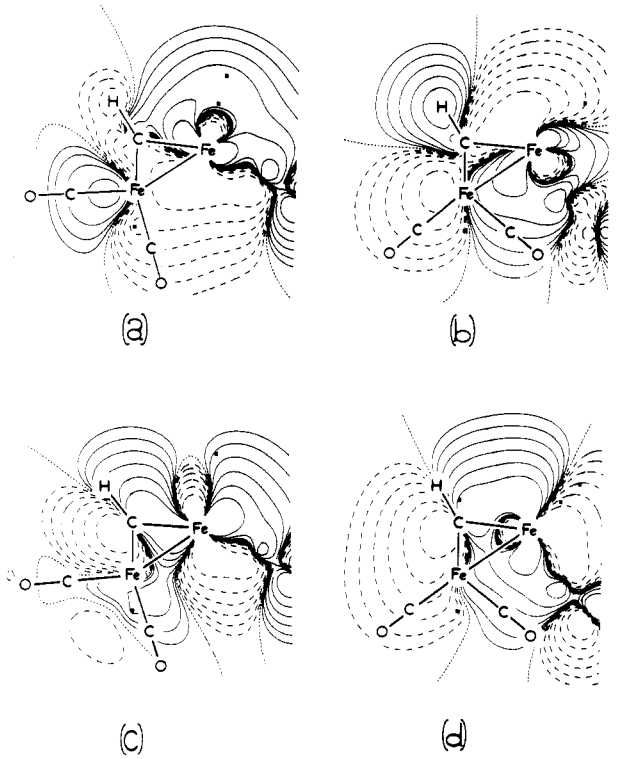

Figure 8. Amplitude contour plots for correlated orbitals in IIIa vs. IIIb: (a) 61 vs. (b) 61 and (c) 58 vs. (d) 59. All are plotted in the *yz* plane containing Fe_2, C, and H atoms and the midpoint of the Fe_1Fe_3 bond. All atoms out of the plane are projected into the specified plane. The positions of two of the carbonyl groups attached to Fe_1 and Fe_3 are indicated to show the structural change in going from IIIa to IIIb. All other atomic positions are indicated by asterisks. Each plot has six contours, each succeeding contour differing from the last by a factor of 2. The largest contour is 0.05 au^{-3}.

Table I. Percent Fe and CH Character of Orbitals in $HFe_3(CO)_9CH^{2-}$

fragment orbital	% (Fe_1 + Fe_3)[a]	% Fe_2[b]	% CH or % C
61 (HOMO)	30	38	2
60	44	21	
59	10	34	17[c]
58	48	8	14[c]
57	32	16	10
50	24	28	37[c]
49	42	5	36[c]
47	24	12	60

[a] Fe_1 and Fe_3 become hinge atoms in the tetrairon butterfly of Ia. [b] Fe_2 becomes a wing tip atom in Ia. [c] H lying in a nodal plane.

the amplitude maps for the correlated orbitals (61 and 58) in IIIa illustrates the dramatic effect of twisting two of the basal iron tricarbonyl units. Thus, the face is "opened up" and becomes an attractive site for the electrophilic attack.

Figure 6 also shows a correlation of the orbitals in IIIb with those of $Fe(CO)_3^{2+}$.[34] Note that the major interaction orbitals are 47, 49, and 50 (the principal triiron–CH cluster orbitals), 60 (trimetal bonding), and the four orbitals perturbed by the carbonyl twisting (57–59 and 61). All these orbitals are shown schematically in Figure 9 and their percentage compositions are listed in Table I. Table II gives the percentage composition of MO's 62–79 in Ia and these data indicate the simplicity of the $HFe_3(CO)_9CH^{2-}/Fe(CO)_3^{2+}$ interaction. Orbital 60 of IIIb has no CH character and interacts with the $19\pi_x$ orbital of $Fe(CO)_3^{2+}$, generating the tetrametal butterfly δ-bonding MO 78. With only one or two exceptions, the principal HFe_4CH–core-cluster-bonding MO's in Ia (i.e., those listed in Table II) retain the fragment orbital properties of *individual* HFe_3CH–core-bonding orbitals of IIIb. Thus, the $Fe(CO)_3^{2+}$ fragment "plugs into" one face of the triiron residue while causing minimal orbital perturbation of either fragment; i.e., the trimetal–alkylidyne interaction constitutes a principal part of the bonding in Ia. In fact the primary cluster-bonding orbitals (47,49, and 50) of IIIb are readily identified as MO's in the tetrairon complex (62,65, and 64) even though 64 involves a significant contribution from the 18σ orbital of the incoming $Fe(CO)_3^{2+}$ fragment.

The HOMO of Ia is generated by a simple interaction between fragment orbitals 61 (HOMO of IIIb) and $20\pi_z$ of $Fe(CO)_3^{2+}$. By considering the representations of these orbitals in Figures 6 and 9, along with the amplitude contour plot of 61 in Figure 8, the evolution of a wing tip iron to hydrogen interaction is nicely evidenced. Thus the

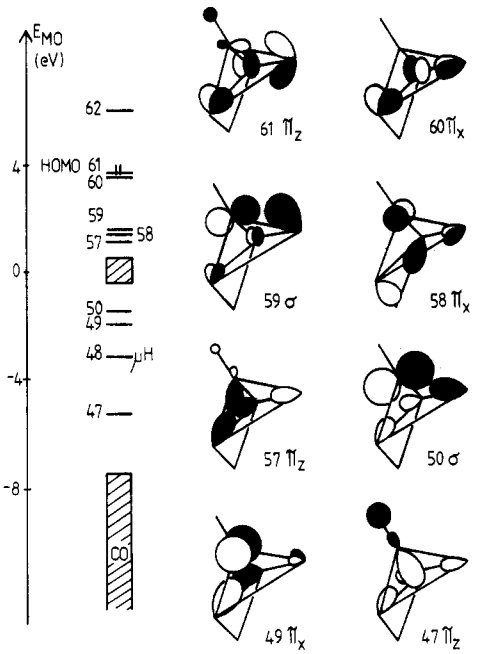

Figure 9. Schematic representation of the triiron–alkylidyne cluster bonding orbitals in $HFe_3(CO)_9CH^{2-}$, IIIb.

Table II. Percent Composition[a] of $HFe_4(CO)_{12}CH$ MO's in Terms of the Fragment Orbitals of $HFe_3(CO)_9CH^{2-}$ and $Fe(CO)_3^{2+}$

MO in Ia	% $HFe_3(CO)_9CH^{2-}$, orbitals, and symmetries	% $Fe(CO)_3^{2+}$, orbitals, and symmetries
79 (HOMO)	71% 61 (π_z)	21% 20 (π_z)
78	55% 60 (π_x); 11% 58 (π_x)	31% 19 (π_x)
77	77% 59 (σ); 8% 57 (π_z)	8% 21 (σ); 6% 18 (σ)
76	69% 57 (π_z)	6% 21 (σ); 6% 20 (π_z); 9% 18 (σ)
75	78% 58 (π_x)	9% 19 (π_x)
65	90% 49 (π_x)	8% 16 (π_x)
64	63% 50 (σ); 6% 48 (μ-H)	22% 18 (σ)
63	93% 48 (μ-H)	
62	93% 47 (σ)	

[a] Contributions $\leq 5\%$ have been ignored.

(34) Note that the expected ordering into t_{2g}, e, and a_1 orbital sets is not immediately apparent. This is simply a function of the axis set, chosen for the $HFe_4(CO)_{12}X$ cluster and defined in Figure 1.

Table III. Summed Orbital Energies for $HFe_4(CO)_{12}CH$ and $HFe_4(CO)_{13}^-$

structure	Fenske-Hall total orbital energy, eV	relative Fenske-Hall energy, eV	relative HOMO energy, eV
Ia	−1682.01	−1.92	−0.12
Ib	−1680.09	0.00	0.00
IIa	−1404.41	−3.26	−0.84
IIb	−1401.15	0.00	0.00

terminal hydrogen of the alkylidyne unit associates itself with the Fe atom as the capping fragment is introduced.

Although the $HFe_3(CO)_9CH^{2-}/Fe(CO)_3^{2+}$ fragment analysis gives a useful bonding picture of Ia in terms of the retention of the HFe_3CH cluster core as a primary bonding unit, it does not indicate clearly what happens to the CH moiety itself as it interacts with the four metal atoms. If one is to use $HFe_4(CO)_{12}CH$ as a model to understand how a hydrocarbon C–H bond is perturbed at a tetrametal site on a metal surface,[12,13] then a bonding analysis in terms of the $HFe_4(CO)_{12}^+$ and CH^- fragments is more appropriate. In the same vein, $HFe_4(CO)_{13}^-$ is viewed in terms of the interaction of $HFe_4(CO)_{12}^+$ with CO^{2-}.

III. Ligand Coordination to a Four-Metal Site. I and II share a common four-metal fragment, $HFe_4(CO)_{12}^+$.[35] The Fenske–Hall transformation of complex MO's into fragment orbitals allows one to explore the binding of a ligand (e.g., CH^- or CO^{2-}) to the metal fragment in terms of the following calculated quantities: (i) orbital energies and compositions (Table III), (ii) orbital symmetries and compositions, (iii) fragment–ligand Mulliken overlap populations (Tables IV and VI), and (iv) Mulliken population changes (Table V). For I and II there are two fundamental questions: how is the ligand affected by interaction with the metal fragment, and how does ligand orientation with respect to the metal fragment (i.e., Ia vs. Ib and IIa vs. IIb) influence ligand bond activation? Here, we focus on the second question. But, before analyzing the ways in which $HFe_4(CO)_{12}^+$ orbitals interact with those of CH^- or CO^{2-}, we point out an obvious difference between these two ligands. In CH^-, orbitals of π symmetry contain no contribution from the H atom. In CO^{2-}, all orbitals (π and σ) include contributions from *both* ligand atoms. Thus, we expect differences in the answer to the question of ligand bond activation since changes in ligand π-orbital population can be significant for the C–O but not the C–H bond.

$HFe_4(CO)_{12}^+$. The orbital properties of the fragment $HFe_4(CO)_{12}^+$ have previously been presented[6,23] but are summarized here for convenience. The metal-fragment orbitals (Figure 10) can be divided into low-lying metal–carbonyl orbitals, a unique Fe_1–H–Fe_3 bridge bonding orbital (61), a set of twelve metal-containing orbitals (62–73), eight "frontier" orbitals (74–81)[36] of which 76 is the HOMO, and high-lying antibonding orbitals. Orbitals 74 and 81 have δ symmetry (see Method section for nomenclature); 77 and 80 have σ symmetry although it is noted that 77 has predominantly wing character. The remaining four orbitals have either π_x or π_y symmetry. The ordering of orbitals 74–81 in Figure 10 is not a simple function of nodal properties. The percentage of M–CO contributions varies with each orbital,[6] and with it the

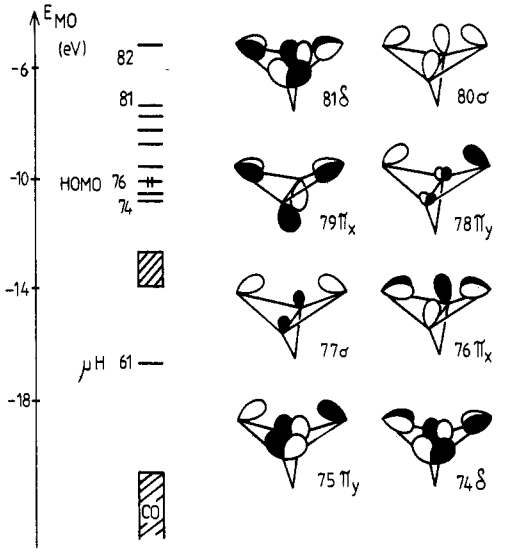

Figure 10. Schematic representation of the frontier orbitals of the $HFe_4(CO)_{12}^+$ butterfly fragment.

effects of metal carbonyl bonding/antibonding character on the orbital energy. In both I and II, orbitals 74, 79, and 81 of the metal butterfly are nonbonding with respect to the ligand; this is analogous to the situation of $HFe_4(CO)_{12}BH_2$[6] with 79 becoming the LUMO of each complex. This leaves orbitals 75(π_y), 76(π_x), 77(σ), 78(π_y) and 80(σ) as the major interaction orbitals with those of each ligand. Restricting our considerations to ligand orientation allows orbital 76 to be dropped from the list. On tilting the CH^- ligand (Ib to Ia), the CH pivots about the x axis, leaving interactions of π_x-orbital symmetry unaffected since the H atom lies in a nodal plane. On tilting the CO^{2-} ligand (IIb to IIa), the ligand again pivots about an x axis through the C $2p_x$ orbital, but the O atom, unlike the H, has a $2p_x$ function. Thus, the interaction of fragment orbital 76 with the CO^{2-} π_x orbitals can be affected by ligand tilting. Tables IV and VI show no change in the (76–1π) overlap in going from Ib to Ia, but there are small changes in (76–1π_x/2π_x*) overlaps in going from IIb to IIa. These changes are virtually self-cancelling, and hence, so far as ligand orientation is concerned, only metal fragment orbitals of π_y and σ symmetry need be considered.

$HFe_4(CO)_{12}CH$. Orbital Energies. From an energetic point of view, there are no large MO stabilizations on going from Ib to Ia (see Figure 2 of ref 23). Likewise, the summed filled-orbital energies listed in Table III suggest Ia as only slightly favored (1.9 eV) over Ib, and the HOMO of the complex is only marginally stabilized (0.12 eV) on tilting the ligand. Clearly, the preference for a tilted ligand orientation over a vertical one (Ia vs. Ib) is a delicate balance of small factors and will not be easily accounted for.

Orbital Symmetries and Compositions. Figure 11 correlates the orbitals of $HFe_4(CO)_{12}^+$ and CH^- with those of complex Ia. A comparative correlation for Ib can be found in ref 23. The CH^- 1σ orbital (not included in Figure 11) interacts with fragment orbital 80, and the evolved MO is found in the metal carbonyl band of both Ia and Ib. Of primary significance is that tilting the ligand with respect to the metal butterfly lowers the symmetry of I from C_{2v} (Ib) to C_s (Ia), thus allowing fragment–ligand σ/π-orbital mixing to occur. Hence, orbital interactions that are disallowed in Ib are allowed in Ia. In Ib, the CH^- 2σ orbital interacts with fragment orbitals 77 and 80. Interaction is straightforward, yielding two complex MO's, 62 and 76, that are fully cluster bonding. Tilting the ligand allows

(35) There are slight changes in the butterfly internal dihedral angle and in the positions of the carbonyl ligands from one complex to another.

(36) Orbital 82 of the $HFe_4(CO)_{12}^+$ fragment has not been included as a "frontier orbital" since its involvement in interaction with CH^- or CO^{2-} orbitals was shown to be relatively unimportant.

Table IV. Fragment Mulliken Overlap Populations[a] of $HFe_4(CO)_{12}^+$ and CH^- in $HFe_4(CO)_{12}CH$

orbital in $Fe_4(CO)_{12}^+$ fragment	orbitals in CH^-					change in overlap per $HFe_4(CO)_{12}^+$ orbital in Ib to Ia[b]
	1σ	2σ	$1\pi(x)$	$2\pi(y)$	$3\sigma^*$	
80 (σ)	−0.043 (−0.021)	0.158 (0.123)				−0.013
78 (π_y)		(0.040)		0.219 (0.166)		−0.013
77 (σ)		0.093 (0.094)		(0.048)		+0.049
76 (π_x)			0.217 (0.217)			0.000
75 (π_y)				0.017 (0.008)	(0.017)	+0.008
change in overlap per CH^- orbital in Ib to Ia[b]	+0.022	+0.006	0.000	−0.014	+0.017	total gain = +0.031

[a] Values in parentheses refer to overlaps in Ia; values not in parentheses refer to Ib. [b] Positive quantity indicates an overlap gain in going from Ib to Ia.

Table V. Ligand Orbital Mulliken Populations: Free Ligand vs. Coordinated Ligand

	CH^- orbitals				
	1σ	2σ	1π	2π	$3\sigma^*$
free CH^-	2.0	2.0	1.0	1.0	0.0
Ia	2.054	1.364	1.028	1.165	0.044
Ib	2.062	1.413	1.028	1.132	0.010

	CO^{2-} orbitals							
	1σ	2σ	$1\pi_x$	$1\pi_y$	3σ	$2\pi_x^*$	$2\pi_y^*$	$4\sigma^*$
free CO^{2-}	2.0	2.0	2.0	2.0	2.0	1.0	1.0	0.0
IIa	2.073	1.952	1.985	1.701	1.475	0.657	0.724	0.810
IIb	2.060	1.953	1.989	1.861	1.445	0.602	0.707	0.008

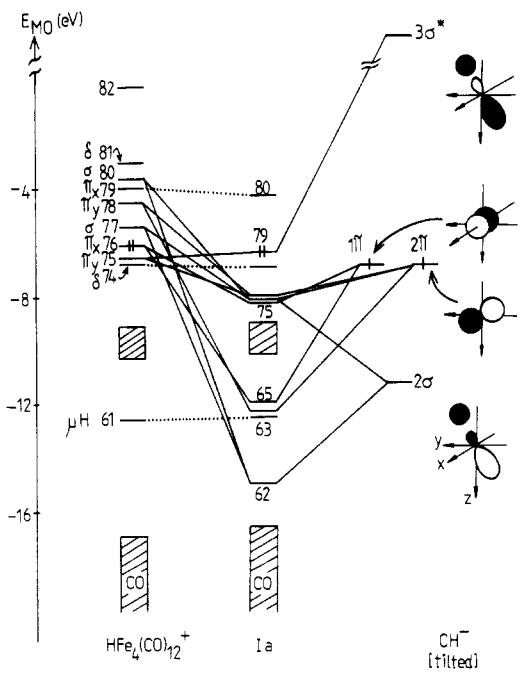

Figure 11. Fragment orbital correlation diagram for the formation of Ia from $HFe_4(CO)_{12}^+$ and CH^-.

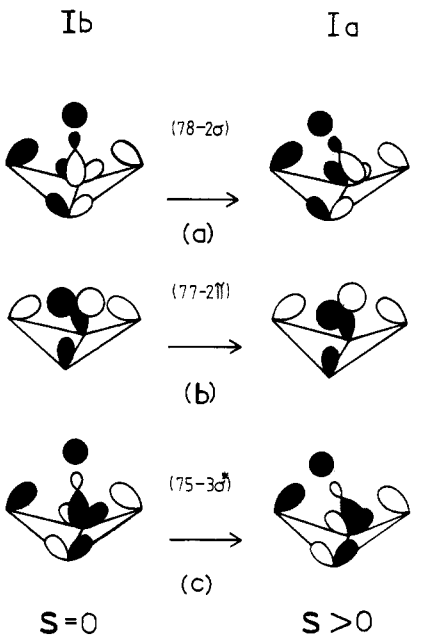

Figure 12. Important $HFe_4(CO)_{12}^+/CH^-$ orbital interactions symmetry disallowed in Ib but allowed in Ia.

the 2σ orbital to interact with $78(\pi_y)$ as well (Figure 12a), thereby generating an Fe(wing)–H–C bonding interaction. The change in complex MO 62 is worth comment. In Ib, the tetrairon butterfly has a total of 8% wing and 26% hinge iron character. The CH sp hybrid accounts for 54% of MO 62, and thus the interaction is mainly with the hinge Fe's. In Ia, MO 62 has 57% CH, 9% each Fe(hinge), 8% Fe_2, and 2% Fe_4. The three Fe atoms of one of the "butterfly wings" therefore interact with the CH sp hybrid in a manner resembling a triiron–alkylidyne residue.[26]

Figure 12b illustrates how tilting the ligand allows the $(77–2\pi)$ interaction to be generated, causing $(75/78–2\pi)$ interactions of Ib to become $(75/77/78–2\pi)$ in Ia. Note that the newly acquired interaction is reminiscent of a triiron-capping carbon e symmetry MO.[26b]

Table VI. Fragment Mulliken Overlap Populations[a] of $HFe_4(CO)_{12}^+$ and CO^{2-} in $HFe_4(CO)_{13}^-$

orbital in $HFe_4(CO)_{12}^+$ fragment	orbitals in CO^{2-} ligand						change in fragment–fragment overlap per $HFe_4(CO)_{12}^+$ orbital
	2σ	$1\pi_x$	$1\pi_y$	3σ	$2\pi_x^*$	$2\pi_y^*$	
80 (σ)	0.007 (−0.006)		(0.020)	0.193 (0.189)			+0.003
78 (π_y)	(0.008)		−0.015 (0.100)	(0.014)		0.112 (0.035)	+0.060
77 (σ)	0.001 (0.007)		(0.003)	0.030 (0.011)		(0.113)	+0.103
76 (π_x)		−0.049 (−0.044)			0.163 (0.157)		−0.001
75 (π_y)			−0.008 (−0.003)	(−0.005)		0.054 (0.035)	−0.019
change in overlap on tilting ligand per ligand orbital[b]	+0.001	+0.005	+0.143	−0.014	−0.006	+0.017	total gain = +0.146

[a] Numbers in parentheses refer to IIa; numbers without parentheses refer to IIb. [b] Positive quantity indicates a net gain in overlap on tilting the ligand.

The $3\sigma^*$ orbital of the CH^- ligand would ordinarily be ignored in the interaction of CH with a cluster fragment since it is high lying, 44 eV above the degenerate HOMO's of the ligand in its coordination geometry.[37] Indeed, analysis of Ib indicates no participation of the $3\sigma^*$ orbital. In going from Ib to Ia $3\sigma^*$ can interact with fragment orbital 75 (Figure 12c) and the HOMO picks up 1.8% $3\sigma^*$ character, leading to the small stabilization noted above. This is a small effect, but as the observed geometry of I is the result of a balance of small effects, it is a significant one. In addition, the participation of the $3\sigma^*$ orbital on tilting provides a ready mechanism for the dissociation of the C–H bond; i.e., further increase in the C–H bond length will increase the interaction of the empty $3\sigma^*$ with the filled orbital 75. Thus the reduction of symmetry on tilting opens a channel for populating the C–H antibonding orbital. This supports the suggestion of Ia as a realistic model for the dissociation of CH on a metal surface.[12,13]

Fragment–Ligand Mulliken Overlap Populations. Table IV lists $HFe_4(CO)_{12}^+/CH^-$ Mulliken overlap populations in Ia and Ib for interactions involving fragment orbitals 75–78 and 80. The right-hand column of Table IV gives an indication of the importance of each metal-fragment orbital in determining a preference for Ia over Ib, while the effect on each ligand orbital in going from Ib to Ia can be seen in the bottom row of overlaps. The net gain in fragment–ligand overlap on tilting the CH^- ligand is marginal. Gains in overlap due to the interactions depicted in Figure 12 are substantial but they are at the expense of (80–2σ), (78–2π), and (75–2π) interactions. Note that the (75–$3\sigma^*$) interaction in Ia, though small, is significant relative to the net preference for Ia.

Mulliken Population Changes. In Table V we compare the ligand orbital populations in free CH^- with those in Ia and Ib. Two observations should be noted. First, irrespective of the ligand orientation, the major effect is charge transfer from the filled CH^- 2σ bonding orbital to the metal fragment. Second, in going from Ib to Ia the changes are much smaller and the total of 0.057 electrons lost from $1\sigma/2\sigma$ orbitals is comparable to the 0.034 electrons gained by the $3\sigma^*$ orbital. Hence, even though the C–H antibonding orbital is relatively high in energy, its participation in ligand activation in Ia cannot be ignored. Though there is little absolute difference between the two ligand orientations, the (75–$3\sigma^*$) interaction that contributes to stabilization of the observed geometry is also responsible for some degree of CH bond weakening.

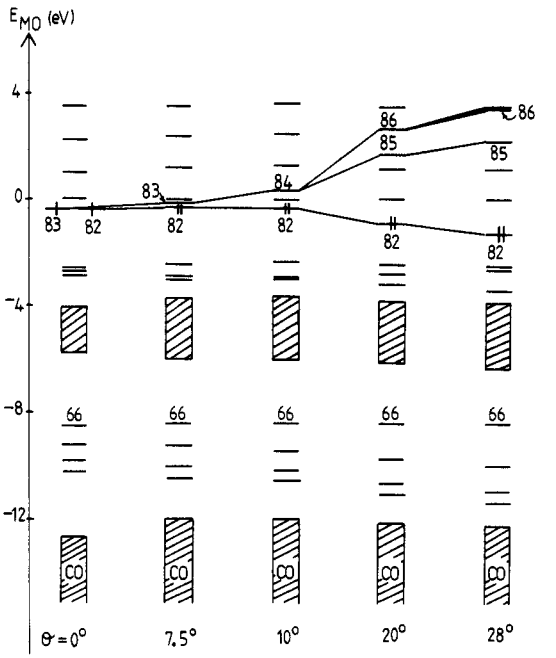

Figure 13. Orbital energy changes accompanying the tilting of the CO^{2-} ligand with respect to the $HFe_4(CO)_{12}^+$ butterfly fragment. The tilt angle θ is defined as the angle between the metal butterfly C_2 axis and the CO bond vector. The correlation lines indicate the major changes in orbital energies. Other correlations are straightforward.

$HFe_4(CO)_{13}^-$. Orbital Energies and Compositions. In marked contrast to the change from Ib to Ia, the orbital energetics accompanying the transition from IIb to IIa (Figure 1) do show dramatic stabilization effects. In IIa, the angle (θ) between the C–O bond vector and the metal butterfly C_2 axis is ~28°. Figure 13 shows the progressive effect on the molecular orbital energies in II as θ is increased from 0° (IIb) to 28° (IIa). In IIb, MO's 82 and 83 are virtually degenerate,[38] but as the CO ligand is tilted,

(37) The Fenske–Hall method tends to exaggerate the differences in orbital energies. For CH^- (1.19 Å) the $3\sigma^*$ orbital lies 44.0 eV above the degenerate HOMO's by Fenske–Hall results but only 16.0 eV above from extended Hückel results.

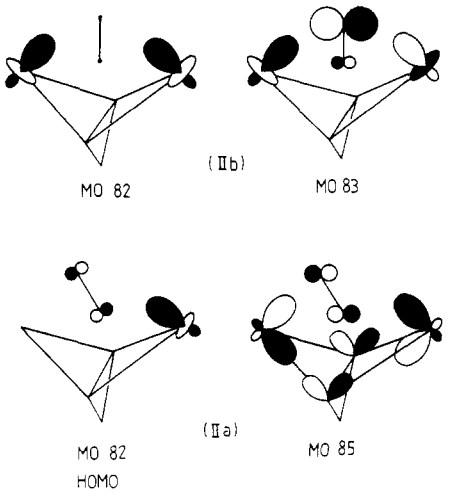

Figure 14. Schematic representations of the accidentally degenerate HOMO pair of orbitals in IIb compared with the corresponding orbitals in IIa.

these two MO's split apart with 82 becoming a well-defined HOMO of the complex even when the tilt angle is set at only a few degrees (exemplified in Figure 13 by $\theta = 7.5°$). MO's 82 and 83 are illustrated schematically in Figure 14. MO 82 has σ symmetry and is derived from orbitals 77 (83%) and 80 (14%) of $HFe_4(CO)_{12}^+$ with no ligand contribution; MO 82 is therefore nonbonding with respect to the $HFe_4(CO)_{12}^+/CO^{2-}$ interaction. MO 83 has π_y symmetry (45% 78 and 18% 75 $HFe_4(CO)_{12}^+$) with a ligand contribution that nets 27% oxygen and only 5% carbon character. This inequality arises from the mixing of the CO^{2-} $1\pi_y$ (9%) and $2\pi_y^*$ (23%) orbitals, and from fragment–ligand Mulliken overlap populations MO 83 is $HFe_4(CO)_{12}^+/CO^{2-}$ antibonding. Thus, the net situation for the HOMO set is unfavorable. Tilting the ligand destroys the C_{2v} symmetry of the molecule (IIb) and allows σ-/π_y-orbital mixing. MO 82 picks up ligand character and becomes metal-fragment–ligand bonding (Figure 14).[39] At the same time as 82 is stabilized, 83 rises in energy removing metal–ligand (78–$1\pi_y$) antibonding character from the HOMO, to empty high-lying MO's 85–90 (exemplified in Figure 14 by MO 85). From the summed orbital energies in Table III, the stabilization of the HOMO is noted to account for 26% of the total MO stabilization that occurs in going from IIb to IIa. We suggest that the primary cause for ligand tilting in $HFe_4(CO)_{13}^-$ is the need for the HOMO to relieve itself of a significant antibonding interaction, (78–$1\pi_y$). The following supports this conclusion.

Orbital Symmetries and Compositions. Figure 15 correlates the orbitals of $HFe_4(CO)_{12}^+$ and CO^{2-} with those in IIa. In IIa, as in Ia, the generation of fragment–ligand interactions that were symmetry disallowed in IIb are of significance, and Figures 16a–c depict three of these interactions. The (78–2σ/3σ) interactions are analogous to the metal–alkylidyne σ-type interaction observed in Ia (Figure 12a). While the (77–$2\pi_y^*$) interaction of IIa (Figure 16c) parallels the (77–2π) combination in Ia (Figure 12b) so far as the ligand carbon atom is concerned, the π-orbital contribution made by the oxygen contrasts with the nodal

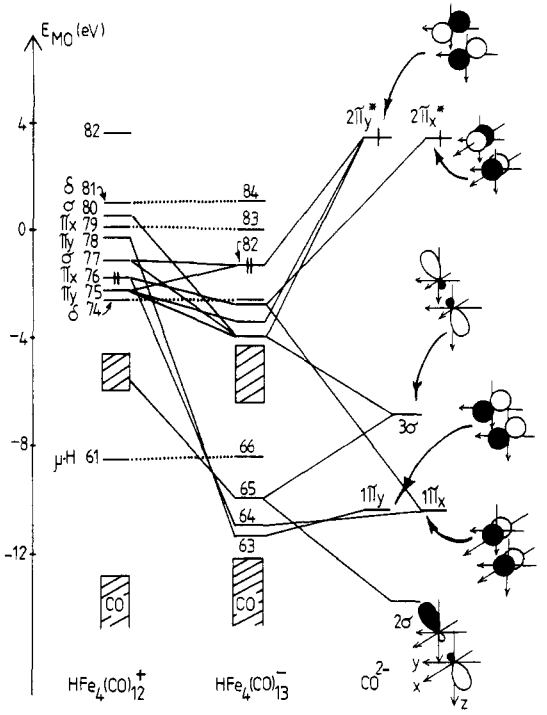

Figure 15. Fragment orbital correlation diagram for the formation of $HFe_4(CO)_{13}^-$ (IIa) from $HFe_4(CO)_{12}^+$ and CO^{2-}.

property of the hydrogen in the CH^- 2π orbital. Figure 16c illustrates how a Fe(wing)–O bonding interaction can be established while the C atom π-bonds to the metal triangle of one butterfly wing. Moreover, the incorporation of a C–O antibonding orbital will induce ligand bond weakening. The (78–$1\pi_y$) bonding interaction (Figure 16d) is also exemplary of the way in which ligand tilting brings about a Fe(wing)–O bonding interaction by virtue of an oxygen π contribution. Thus, from a consideration of orbital symmetries, the $HFe_4(CO)_{12}^+/CO^{2-}$ orbital combinations in IIa appear to have a greater potential for setting up an Fe–X–C (X = H or O) bridge than $HFe_4(CO)_{12}^+/CH^-$ orbital interactions in Ia.

Fragment-Ligand Mulliken Overlap Populations. Table VI lists $HFe_4(CO)_{12}^+/CO^{2-}$ Mulliken overlap populations. Inspection of the values shows two major fragment–ligand overlap gains as the ligand tilts: (78–$1\pi_y$) and (77–$2\pi_y^*$) (Figure 16). (78–$1\pi_y$) goes from being antibonding in IIb to bonding in IIa. This change is directly correlated to the HOMO–LUMO splitting described earlier. The (78–$1\pi_y$) interaction appears in MO's 63 and 83 in IIb and in MO's 63, and 85–90 in IIa. (78–$1\pi_y$) overlap in MO 63 is constant and unaffected by ligand tilting. The change in net (78–$1\pi_y$) overlap noted in Table VI arises from the loss of substantial antibonding character present in MO 83 of IIb to empty MO's (85–90) in IIa. As far as the CO^{2-} ligand is concerned, the gain in fragment–ligand overlaps involving the $1\pi_y$ orbital is the overwhelming factor determining the preference of IIa over IIb; Table VI indicates a total gain in Mulliken overlap population of 0.146, 98% of which comes from CO^{2-} $1\pi_y$ interactions, 78% being attributed to the change from (78–$1\pi_y$) bonding to antibonding contribution.

The final column in Table VI shows the change in overlap per $HFe_4(CO)_{12}^+$ orbital in going from IIb to IIa. Besides reiterating the role of orbital 78, the values indicate the importance of orbital 77. A consideration of orbital symmetries has already shown that tilting the ligand allows 77 to interact with ligand orbital $2\pi_y^*$ (Figure 16c). Mulliken overlap populations suggest that this interaction

(38) In the Fenske–Hall results, MO's 82 and 83 are considered as a degenerate HOMO set. The degeneracy is accidental and appears to be method dependent; the results of an extended Hückel calculation place the energies of the corresponding MO's in IIb further apart, but the same trend in MO separation as is depicted in Figure 13 is observed in both the extended Hückel and Fenske–Hall results.

(39) Note that the combination of fragment orbitals 75 and 77 wipes out one of the wing tip iron contributions.

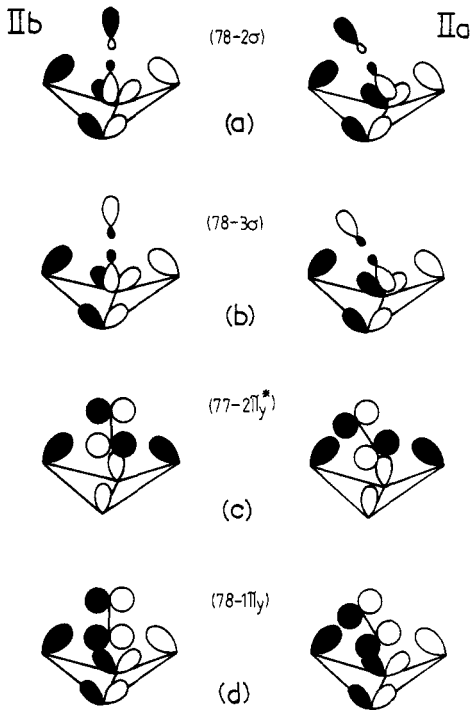

Figure 16. Important $HFe_4(CO)_{12}^+/CO^{2-}$ orbital interactions in IIa. (a), (b), and (c) show interactions disallowed in IIb but allowed in IIa.

is significant, but it should be noted that 85% of the ($77-2\pi_y^*$) overlap gain merely compensates for loss in ($75/78-2\pi_y^*$). Changes in fragment–ligand overlaps involving CO^{2-} σ orbitals are relatively unimportant.

Mulliken Population Changes. In Table V we compare ligand orbital populations in IIa, IIb, and free CO^{2-}. By far the greatest change in population is the charge lost by the $1\pi_y$ (C–O bonding) orbital; 0.160 electrons are transferred to metal-fragment orbitals on tilting the ligand. At the same time the $2\pi_y^*$ and the $2\pi_x^*$ orbitals gain 0.017 and 0.055 electrons, respectively. All three changes will result in a weaker C–O bond. Hence we observe CO π and π^* orbitals predominating over the σ orbitals as a means of activating the C–O bond upon coordinating the ligand to the metal fragment. Further, this phenomenon can only take place when the ligand is bound asymmetrically between the wing tips of the metal butterfly.

IV. Summary. In exploring the ligand binding of CH^- and CO^{2-} to the $HFe_4(CO)_{12}^+$ fragment, we have considered changes in MO energies and compositions, orbital symmetries, fragment–ligand Mulliken overlap populations, and changes in orbital populations in an effort to delineate the preferred ligand geometry and the mechanism of ligand bond activation. We conclude that there are some similarities between the fragment–ligand binding in I and II. As the ligand tilts, orbital mixing is allowed and there arise parallel metal–ligand interactions, e.g., ($78-2\sigma$) in Ia vs. ($78-2\sigma/3\sigma$) in IIa. In both cases, metal-fragment–ligand interactions can be identified that allow an effective bonding description of $HFe_4(CO)_{12}X$ compounds to be based on an Fe_3X (X = CH or CO^-) core, thus corroborating the simple geometrical argument. However one primary distinction between the ligands (viz., the availability of π orbitals on oxygen but not on hydrogen) gives rise to a fundamental difference between them. In I, the $HFe_4(CO)_{12}^+/CH^-$ orbital interactions are finely balanced between Ia and Ib. There is a small net gain in metal-fragment–ligand Mulliken overlap population as the ligand tilts, but there are no dramatic changes in any of the corresponding MO parameters in Ia and Ib. In contrast, large changes in certain MO parameters are observed in going from IIb to IIa, rationalizing the known preference of IIa over IIb. Although mere coordination of a ligand to a metal cluster fragment (or, by analogy, to a metal surface) may cause activation, e.g., CO, our results also indicate that ligand orientation with respect to the metal fragment can be an important factor in either weakening bonds in the coordinated ligand or providing a route for such weakening. This substantiates previous suggestions[12,13]. Finally, it should be noted that we have also performed Fenske–Hall calculations on I and II using structures Ic and IIc (Figure 1) with the ligand C atom lying closer to one Fe(wing) atom as found experimentally. However we cannot explain the greater stabilities of these structures (i.e., Ic vs. Ia and IIc vs. IIa) unless detailed analyses of intra- as well as interfragment bonding is included.

Table VII. Idealized Geometries (Å) for $HFe_4(CO)_{12}X$ (Figure 1)

X	Fe_1-C and Fe_3-C	Fe_2-C and Fe_4-C	C-H or C-O	Fe_4-H or Fe_4-O
CH (Ia)	1.94	1.95	1.19	1.75
CH (Ib)	1.94	1.95	1.19	1.95
CO (IIa)	2.03	1.96	1.26	1.94
CO (IIb)	2.03	1.96	1.26	2.48

Method

Fenske–Hall calculations were carried out on complexes $HFe_4(CO)_{12}CH$ (I) and $HFe_4(CO)_{13}^-$ (II). The geometry of the $HFe_4(CO)_{12}$ unit was idealized to C_{2v} symmetry with an internal dihedral angle of 114° (α in Figure 1). This value lies midway between the experimental values for I and II (111° and 117°, respectively) and is equal to the dihedral angle in $HFe_4(CO)_{12}BH_2$.[6] All Fe(wing)–Fe(hinge) distances were 2.66 Å and Fe(hinge)–Fe(Hinge) was 2.62 Å. All terminal C–O lengths were set at 1.13 Å and Fe–CO lengths at 1.80 Å. The hinge bridging H was on the butterfly C_2 axis and Fe(hinge)–μ-H = 1.66 Å. In the crystallographically determined structures of I[1] and II[5] the carbon atom of each ligand is asymmetrically positioned between the wing tip Fe atoms of the metal fragment (Figures Ic and IIc). For the purpose of this work, the carbon was equidistant between the wing tips. Two structures were considered for each complex: Ia and IIa (Figure 1) have the ligand in a tilted orientation such that the known C–H and H–Fe or C–O and O–Fe distances are reproduced (Table VII); Ib and IIb (Figure 1) are hypothetical structures retaining the C_{2v} symmetry of the $HFe_4(CO)_{12}^+$ fragment with the CH^- or CO^{2-} ligand positioned vertically and using the experimental Fe–C and C–H or C–O distances (Table VII).

The Fenske–Hall calculations employed single-ζ Slater functions for the 1s and 2s functions of C and O. The exponents were obtained by curve fitting the double-ζ functions of Clementi[40] while maintaining orthogonal functions; the double-ζ functions were used directly for the 2p orbitals. For H, an exponent of 1.16 was used. The Fe 1s–3d functions were taken from the results of Richardson et al.[41] and were all single-ζ except for the 3d function which was double-ζ and was chosen for the +1 oxidation state. Both the 4s and 4p exponents were taken as 2.00.

Throughout the calculations, the same axes are retained (Figure 1). When considering the interaction of $HFe_4(CO)_{12}^+$ with CH^- or CO^{2-}, all metal-fragment orbitals are given labels that refer to symmetry with respect to a ligand on the C_2 axis on the tetrairon butterfly, namely, σ, π_x, π_y, and δ. When the ligands are tilted (Ia and IIa), the same ligand orbital labels are used as in Ib and IIb (see Figures 11 and 15). The analysis of $HFe_4(CO)_{12}CH$ in terms of $HFe_3(CO)_9CH^{2-}$ and $Fe(CO)_3^{2+}$ uses orbital labels that are based on the approach of the $Fe(CO)_3^{2+}$ fragment to the Fe_1Fe_3C face contained in the xz plane (Chart I). Using the

(40) Clementi, E. *J. Chem. Phys.* **1964**, *40*, 1944.
(41) Richardson, J. W.; Nieuwpoort, W. C.; Powell, R. R.; Edgell, W. F. *J. Chem. Phys.* **1962**, *36*, 1057.

original axes (Figure 1) and considering nodal planes with respect to the y axis gives σ, π_x, and π_z labels. Note that orbitals of the triiron fragment of π_z symmetry will include a contribution from the terminal H atom that lies in the yz plane (Chart I and Figure 9).[42]

(42) It would be more usual to denote the triiron fragment orbital symmetries with respect to the C_3 axis of the Fe_3C tetrahedron. The nomenclature chosen here allows the independent orbital analyses of $HFe_4(CO)_{12}CH$ to be compared more easily.

Acknowledgment. The support of the National Science Foundation under Grant No. CHE 81–09503 is gratefully acknowledged. We also thank the Notre Dame Computing Center for computing time, Professor Roger DeKock for his help with the transformations, and Reynaldo Barreto for his help in running the Fenske–Hall calculations.

Registry No. I, 74792-06-6; II, 62361-87-9; III, 89414-14-2.

Addition Compounds of Alkali-Metal Hydrides. 25. Rapid Reaction of Boronic Esters and Acids with Lithium Aluminum Hydride. A Novel and Quantitative Synthesis of Lithium Monoorganylborohydrides[1]

Bakthan Singaram,[2] Thomas E. Cole, and Herbert C. Brown*

Richard B. Wetherill Laboratory, Purdue University, West Lafayette, Indiana 47907

Received January 20, 1984

Boronic esters readily react with lithium aluminum hydride in diethyl ether–pentane at 0 °C to form the corresponding lithium monoorganylborohydrides and dialkoxyalanes. Under these reaction conditions, the dialkoxyalanes generally precipitate quantitatively from solution. The reaction is essentially quantitative and is broadly applicable to a representative variety of boronic esters. Boronic acids can also be readily converted to the corresponding lithium monoorganylborohydrides by treatment with lithium aluminum hydride. The reaction is quantitative and, like the boronic esters, is broadly applicable to a wide variety of boronic acids. These procedures provide a general, convenient synthesis of lithium monoorganylborohydrides with organic groups of greatly varying steric requirements.

Trialkylborohydrides have been demonstrated to be powerful selective reducing agents[3] and versatile synthetic intermediates.[4] Recently, several important routes to trialkylborohydrides have been developed.[5] In contrast, little effort has been devoted to the chemistry of monoorganylborohydrides, principally the result of the absence of satisfactory synthetic routes for monoorganylboranes. We reported one synthetically useful preparation of pure lithium monoalkylborohydrides[6] by treating triethylenediamine–monoalkylborane complexes ($TED{\cdot}BH_2R$) with lithium aluminum hydride ($LiAlH_4$), giving the borohydride in quantitative yield (eq 1). However, this procedure is limited to those monoalkylborane complexes that can be readily prepared from the reaction of relatively hindered olefins with triethylenediamine–thexylborane adduct ($TED{\cdot}BH_2Th$) (eq 2).

$$TED{\cdot}BH_2R + LiAlH_4 \xrightarrow[1\text{ h}]{\text{THF, 65 °C}} LiRBH_3 + TED{\cdot}AlH_3\downarrow \quad (1)$$

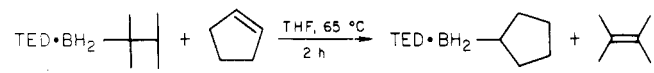

(2)

The reaction of borane–dimethyl sulfide (BMS) with various organolithium reagents has been reported to give the corresponding lithium monoorganylborohydrides (eq 3).[7,8] However, experimental work in our laboratory has

$$Me_2S{\cdot}BH_3 + RLi \rightarrow LiRBH_3 + Me_2S \quad (3)$$

R = Me, *n*-Bu

shown that this reaction produces a mixture of products.[9] More recently, Nöth and co-workers[10] have reported similar results in their systematic investigation of the reaction of organolithium reagents with various borane donors: $THF{\cdot}BH_3$, $Me_2S{\cdot}BH_3$, and $Me_3N{\cdot}BH_3$. Irrespective of the reaction conditions and reagents, all members of the series $LiR_{(4-n)}BH_n$ are present in the product. In few cases were pure lithium monoorganylborohydrides isolated from the reaction mixture in only modest yield.

In the course of our study of the synthesis of dialkylboranes from borinic esters (R_2BOMe), we discovered that

(1) Part 24: Brown, H. C.; Cha, J. S.; Nazer, B. *Organometallics* **1984**, *3*, 0000.
(2) Postdoctoral research associate on Grant CHE-7918881 from the National Science Foundation.
(3) Krishnamurthy, S. *Aldrichim. Acta* **1974**, *7*, 55.
(4) (a) Brown, H. C.; Kim, S. C. *J. Org. Chem.* **1977**, *42*, 1482. (b) Brown, H. C.; Hubbard, J. L. *Ibid.* **1979**, *44*, 467.
(5) Brown, H. C.; Singaram, B.; Singaram, S. *J. Organomet. Chem.* **1982**, *239*, 43.
(6) Brown, H. C.; Singaram, B.; Mathew, C. P. *J. Org. Chem.* **1981**, *46*, 4541.
(7) Kim, S.; Moon, Y. C.; Ahn, K. H. *J. Org. Chem.* **1982**, *47*, 3311.
(8) Kim, S.; Lee, S. J.; Kary, H. J. *Synth. Commun.* **1982**, *12*, 723.
(9) Independent observations by B. Singaram and B. Nazer.
(10) Buffar, W.; Nöth, H.; Sedlak, D. *Organometallics* **1983**, *2*, 579.

0276-7333/84/2303-0774$01.50/0